Spatial transcriptomic analysis of HIV and tuberculosis coinfection in a humanized mouse model reveals unique transcription patterns, immune responses and early morphological alterations

Sitaramaraju Adduri[1#], Jose Alejandro Bohorquez[1#], Rajesh Mani[1], Omoyeni Adejare[1], Diego Rincon2, Joshua K. Kleam[1], Mounika Duggineni[1], Andy Omeje[1], Torry Tucker[1], Nagarjun V Konduru[1], Guohua Yi[1*]

1. Department of Cellular and Molecular Biology, School of Medicine, The University of Texas Health Science Center at Tyler, 11937 US HWY 271, Tyler, TX 75708, USA
2. Unaffiliated pathologist

*Corresponding author: Guohua.Yi@uthct.edu

#Authors contributed equally to this work

Keywords: HIV and tuberculosis coinfection, Humanized mouse model, Early granuloma formation, Spatial transcriptomics, Imaging mass cytometry.

Abstract

Mycobacterium tuberculosis (*Mtb*) and human immunodeficiency virus (HIV) coinfection is one of the biggest public health concerns worldwide. Both pathogens are adept at modulating immune response and, in the case of *Mtb*, even inducing structural modification of the affected tissue. The present study aimed at understanding the early phenotypical and functional changes in immune cell infiltration in the affected organ, using a humanized mouse model. The humanized mice were infected with either HIV or *Mtb* in single infection, or with both pathogens in coinfection. Three weeks after the infection, lung samples were collected, and spatial transcriptomics analysis was performed. This analysis revealed high infiltration of $CD4^+$ T cells in *Mtb* infection, but not in HIV or coinfection. Coinfected mice also showed a minimal number of NK cells compared to the other groups. In addition to infection status, histological features also influenced the immune cell infiltration pattern in the lungs. Two distinct airway regions with distinct immune cell abundance patterns were detected by spatial transcriptome profiling. A lymphoid cell aggregate detected in coinfection lung exhibited distinct transcript profile. The cellular architecture in the lymphoid cell aggregate did not follow the spatial patterns seen in mature granulomas. However, lymphoid cell aggregates exhibited granuloma gene expression signatures, and pathways associated with reactive oxygen species production, oxidative phosphorylation, and TGFβ and interferon signaling similar to granulomas. This study revealed specific transcription patterns, immune responses and morphological alteration signaling in the early stage of HIV and *Mtb* infections.

38 **Introduction**

39 Tuberculosis (TB), caused by *Mycobacterium tuberculosis* (*Mtb*), continues to be a major public
40 health concern. It has been estimated that as much as 25% of the world's population is infected with *Mtb*,
41 although most of these patients will develop the latent form of TB (LTBI)[1]. One of the main features of *Mtb*
42 is its ability to modulate the immune response, facilitating the establishment of latent disease. This immune
43 modulation occurs in circulating immune cells but also extends to resident tissue cells, where *Mtb* is able
44 to induce structural modification in host tissue, forming specialized histological structures known as
45 granulomas[2,3]. These structures are composed of a necrotic core enriched by diverse immune cell
46 populations that contain the pathogen, preventing its spread throughout the host and the development of
47 active TB. Consequently, there is growing interest in studying cellular infiltration in lung tissue during *Mtb*
48 infection, particularly within granulomas[4-6]. Alterations in cellular subsets in the affected organ, coupled
49 with intercellular communication, explain how these alterations either promote or hinder pathogen
50 dissemination. Multiple microenvironments are present within granuloma structures that induce an
51 immunoregulatory environment with differential signaling, characterized by pathway activation and
52 cytokine production, which are critical for maintaining the granuloma structure[7].

53 Local or systemic immune alterations can disrupt granuloma structures, facilitating bacterial
54 growth[8,9]. The human immunodeficiency virus (HIV) is a major driver of the immune dysregulation,
55 destabilizing granuloma structures that are critical for controlling *Mtb*[9]. In individuals coinfected with HIV
56 in *Mtb*, the risk of developing active TB[10] is significantly increased because of profound
57 immunosuppression, primarily driven by the depletion of CD4+ T cells, the main target for HIV infection,
58 including those within granulomas. Reports show that $CD4^+$ T cells within granulomas are particularly
59 susceptible to HIV infection due to increased CCR5 coreceptor expression[8]. Furthermore, as $CD4^+$ cells are
60 essential for $CD8^+$ cell maturation, the HIV-induced $CD4^+$ cell depletion reduces the population of
61 circulating effector and memory $CD8^+$ cells, promotes immunosenescence in these cells, and impairs their
62 functionality[11].

63 Studies dedicated to understanding the cellular composition and intercellular networks present
64 locally in the lungs during *Mtb* infection and HIV/*Mtb* coinfection have focused on infection models or
65 samples in which infections and structural changes are already present in the host, leaving a gap in the
66 knowledge of the early post-infection events[5-8,12]. This is partially due to the use of stored human samples
67 or nonhuman primate (NHP) animal models for these experiments, which, while reliable, offer limited
68 access to early infection timepoints. Recent studies have demonstrated the potential of humanized mice as
69 effective models for studying *Mtb* and HIV[13,14], capable of replicating immune changes caused by infection,
70 including the lung granuloma formation. The present aimed to investigate early changes in the lung's
71 cellular repertoire induced by HIV, *Mtb*, or their coinfection, at an early timepoint in which granulomas
72 have not been fully established. Additionally, we analyzed the transcriptomic changes in these cells using a
73 spatial approach to determine alterations in cytokine production in the affected lung regions, enabling us to
74 characterize the molecular processes that occur during infection and providing evidence of early granuloma
75 development.

76

77 **Materials and methods**

78 **Generation of humanized mice**

79 Mice of the NOD.Cg-Prkdc^{scid} Il2rg^{tm1Wjl} Tg(CMV-IL3,CSF2,KITLG)1Eav Tg(IL15)1Sz/J (NSG-
80 SGM3-IL15) strain (The Jackson Laboratory, Bar Harbor, ME), housed at the University of Texas Health
81 Science Center at Tyler (UTHSCT) animal facility, were used for this study. Four- to five-week-old mice
82 were irradiated at a dose of 100 cGy/mouse for myeloablation. Six hours later, each mouse was
83 intravenously (IV) inoculated with 2×10^5 human CD34$^+$ hematopoietic stem cells (STEMCELL
84 Technologies, Vancouver, Canada) for humanization.

85 At 16 weeks post-inoculation with human CD34$^+$ cells, humanization was confirmed following an
86 established protocol in our laboratory. Briefly, whole-blood samples were collected by puncture of the

87 submandibular vein, and a density gradient was used to separate peripheral blood mononuclear cells
88 (PBMCs). Once PBMCs were obtained, flow cytometry for specific human and mouse immune cell markers
89 was performed, and humanization was confirmed in 13 mice. The criteria for humanization included a
90 positive human/mouse leukocyte ratio, as determined by human $CD45^+$ vs. mouse $CD45^+$ expression, as
91 well as the presence of multiple human immune cell subsets, as determined by markers for T cells ($CD3^+$),
92 B cells ($CD20^+$), monocytes ($CD14^+$) and natural killer (NK) cells ($CD56^+$), as described in our published
93 protocol[13].

94 **Animal infection and experimental design**

95 After confirming successful humanization, the animals were randomly assigned into 4 experimental
96 groups (Figure 1A): A) no infection (n=3), B) HIV single infection (n=3), C) *Mtb* single infection (n=3)
97 and D) HIV/*Mtb* coinfection (n=4). Animals in Groups C and D were infected with aerosolized *Mtb* or the
98 H37Rv strain using a Madison chamber[13,15]. To verify the infection dose, three non-humanized mice were
99 included in the infection chamber, euthanized the following day, and their lung samples were collected,
100 macerated and plated on 7H10 plates supplemented with OADC (BD Biosciences, Franklin Lakes, NJ).
101 These mice confirmed successful infection with an approximate dose of 40 CFU/lung.

102 Two days after *Mtb* infection, the mice in Groups B and D were intraperitoneally (IP) injected with
103 10^7 $TCID_{50}$ of the HIV-1 BaL strain (obtained from the NIH AIDS Reagent Program). Two weeks after
104 inoculation, whole blood samples were obtained, and RNA was extracted from the plasma samples using a
105 NucleoSpin RNA isolation kit (Macherey-Nagel, Allentown, PA) as per the manufacturer's instructions.
106 Viral RNA load in each animal was quantified using RT–qPCR with a control standard of known HIV-1
107 genome copy numbers (obtained from the NIH AIDS Reagent Program), as previously described[16]. All
108 HIV-inoculated mice were positive for HIV via RT–qPCR and presented similar viral RNA loads.

109 Three weeks after infection, all the animals were humanely euthanized in accordance with the NIH
110 guidelines for the euthanasia of rodents with carbon dioxide, with confirmation by cervical dislocation.

111 During necropsy, lung samples from each mouse were collected in accordance with previous protocols.
112 Briefly, once euthanasia was confirmed, the thoracic cavity was opened, and the lungs were perfused and
113 inflated by injection of 10% neutral buffered formalin (Thermo Scientific, Waltham, MA) into the right
114 heart ventricle and trachea, respectively. Afterward, the samples were immediately submerged in the same
115 buffer and kept at 4 °C until paraffin embedding[17,18]. All animal procedures were approved by the UTHSCT
116 Institutional Animal Care and Use Committee (IACUC) (Protocol #763).

117 **10x Visium spatial transcriptome assay:**

118 Formalin-fixed, paraffin-embedded (FFPE) tissue sections were used to prepare sample slides
119 according to the 10x Genomics protocol (CG000518 and CG000520). RNA was extracted from the FFPE
120 sections using the RNeasy FFPE Kit (Qiagen, 73504) according to the manufacturer's protocol. Samples
121 with DV200 values > 30% were selected for spatial transcriptomics assay. After hematoxylin and eosin
122 (H&E) staining and imaging, qualified samples were decrosslinked per protocol (CG000520), and the
123 sequencing libraries were prepared according to the manufacturer's protocol (CG000495). The quality of
124 the final libraries was assessed using the Agilent High Sensitive DNA Kit (5067-4626) with an Agilent
125 Bioanalyzer 2100 (Agilent Technologies, Santa Clara, USA). The qualified libraries were sequenced using
126 paired-end sequencing on an Illumina NovaSeq System (Illumina, Inc., USA).

127 **Visium spatial sequencing data analysis:**

128 With demultiplexed sequence fastq files and CytAssist tissue images as inputs, space ranger was
129 used to map the reads to the latest human genome (hg38) and quantify the read counts per spot. The counts
130 were normalized via the 'sctranform' method in the Seurat package[19]. For cross-sample comparisons, data
131 were further normalized using the minimum median count function. The samples were clustered and
132 projected on UMAP. The "Find marker" function was used to identify cluster-specific markers and
133 differentially expressed genes, defined as genes with a minimum |log2FC| value of 2 at an adjusted p value
134 of <0.05. Pathway analysis was performed using GprofileR[20]. The Loupe browser was used to examine the

spot-wise expression levels of individual genes. Deconvolution of spatial gene expression profiles was performed using the RCTD package[21]. Single-cell RNA sequencing data (GSE192483) of lung tissues with 18F-FDG avidity and nearby uninvolved tissues from six tuberculosis patients[22] were used as a reference for deconvolution analysis. Azimuth[23] was used for annotating the cells in the reference dataset. Visualizations were created using the ggplot2 package in the R environment (4.1.1). Gene set enrichment analysis (GSEA) was performed using the 'fgsea' package with default settings, leveraging C8 datasets from molecular signatures database. The gene sets for human were downloaded into R environment using 'msigdb' package. Differentially expressed genes identified by 'FindMarkers' function of 'seurat' were ranked based on average logFC and adjusted p values were used as input for GSEA. GSEA was performed using 'fgsea' command with 1000 permutations on the ranked list of genes. An adjusted p value of 0.25 was cut off as suggested by the original documentation of the GSEA.

Imaging mass cytometry (IMC):

IMC was performed on 5-micron thick sections from FFPE blocks. The sections were baked at 60^0C for 2 hours and dewaxed in xylene for 20 minutes. The sections were rehydrated in a graded series of ethyl alcohol followed by water. The sections were incubated at 96^0C for 30 minutes in 1x target retrieval solution with pH 9 (Cat #S236784-2, Agilent) and cooled at 70^0C for 20 minutes. The sections were blocked with 3% bovine serum albumin in PBS for 45 minutes at room temperature. An antibody cocktail was applied, and the slides were incubated overnight at 4°C in a hydration chamber. After washing with 0.2% Triton X-100 and with PBS, the sections were counterstained with Ir-Intercalator (cat# 201192A; Standard Biotools) at 1:400 dilution in PBS for 30 min at room temperature. The sections were air dried at room temperature for 20 minutes. Imaging was performed on Hyperion XTi imaging system (Standard Biotools). Regions of interest were selected using CYTOF software, and the data was analyzed using MCD viewer.

Immunofluorescent staining:

158 Formalin-fixed paraffin-embedded (FFPE) lung sections from *Mtb* single-infected and *Mtb*/HIV-
159 coinfected mice were processed for immunofluorescence staining as follows. Tissue sections-containing
160 slides were incubated at 60 °C for 2 hours to melt the paraffin, followed by complete deparaffinization in
161 fresh xylene (4 × 5 min each). Sections were then rehydrated through a graded ethanol series (100%, 95%,
162 70% and 50%; 10 min each) and rinsed in distilled water. Antigen retrieval was performed by incubating
163 slides in 10 mM sodium citrate buffer (pH 6.07) at 90 °C for 1 hour. After cooling to room temperature,
164 nonspecific binding was blocked using the protein concentrate and mouse Ig blocking reagent from the
165 M.O.M. Immunodetection Kit (Vector Laboratories). Sections were then incubated with primary antibodies
166 against surface markers for human CD68 and CD3 (Invitrogen, Thermofisher) and intracellular markers for
167 IRF-7 (Invitrogen, Thermofisher) and TGF-β (Santa Cruz) overnight at 4 °C. The following day, slides were
168 washed and then incubated with anti-mouse secondary antibodies conjugated with AF488, AF568, and
169 AF647 (Invitrogen, Thermofisher) for 2 hours at room temperature. After washing, coverslips were
170 mounted with DAPI-containing medium, and images were acquired on a Zeiss LSM-500 confocal
171 microscope. All micrographs were processed using ImageJ (Fiji, NIH).

172

173 **Results**

174 **Immune cell infiltration patterns in the lungs vary distinctly across each infection type**

175 We generated humanized mice using the NSG-SGM3-IL15 mouse strain. As expected, the
176 expression of human IL-3, GM-CSF, and KITLG genes led to the development a full-lineage of human
177 immune cells, similar to our previously reported humanized NSG-SGM3 mice[24]. Additionally, the
178 transgenic expression of the human IL-15 gene resulted in a substantial portion of differentiated human
179 natural killer (NK) cells (**Figure S1**). Using this humanized NSG-SGM3-IL15 mouse model, we
180 investigated the effect of HIV and *Mtb* coinfection on immune responses in the lungs. In our prior study on
181 a humanized mouse model of coinfection, we observed rapid $CD4^+$ T-cell depletion within 15 days post-

182 infection and plateaued after 28 days. To examine immune responses during the rapid decline of $CD4^+$ cells,
183 we euthanized mice 21 days post-infection and performed spatial transcriptome analysis of lung specimens
184 from humanized mice with HIV infection, *Mtb* infection, and coinfection, using the 10x Genomics Visium
185 platform. The uninfected group served as a control (**Figure 1A**). After excluding the poor-quality regions
186 and empty spots, our spatial transcriptomics analysis detected the expression of 18,000 genes across 3633,
187 2698, 2778, and 1397 spots in uninfected, HIV-infected, *Mtb*-infected, and coinfected lungs, respectively.

188 As TB primarily affects lungs, analyzing the infiltration frequency of various immune cells into
189 lungs is critical to understand the immune response against *Mtb*. $CD4^+$ T cells play crucial roles in
190 controlling *Mtb* infection by releasing signals that activate B cells to produce antibodies, cytotoxic T cells
191 to eliminate infected cells, and macrophages to engulf and destroy pathogens. Consequently, we sought to
192 investigate how reduced $CD4^+$ T cell levels impact immune cell infiltration in lung tissues during *Mtb*/HIV
193 coinfection. To compare the abundance of immune cell markers across all 4 infection groups, we normalized
194 spatial gene expression data from all samples using the sctranform method and then corrected the minimum
195 median counts of the SCT data to ensure comparability across samples. As shown in **Figure 1B**, expression
196 of CD45 (PTPRC gene) is elevated in lung tissue from *Mtb* single infection compared to all other infection
197 groups. CD45 is expressed in all nucleated lymphoid cells and over expression of CD45 indicates excessive
198 immune cell infiltration in *Mtb* lungs compared to others. Next, we observed minimal CD4 expression in
199 the HIV single infection and coinfection groups compared with the uninfected and *Mtb* single infection
200 groups, consistent with HIV-driven massive depletion of $CD4^+$ T cells (**Figure 1C)**. These results suggest
201 an infection-specific landscape of immune cell infiltration in the lungs.

202 To further investigate immune cell infiltration frequencies in the lungs across different infection
203 groups and controls, we performed RCTD-based cell type deconvolution analysis by integrating previously
204 published single-cell RNA sequencing data of human lung granulomas (as detected by PET-CT) and their
205 matched normal tissues from TB patients with our spatial transcriptome data from all 4 infection groups:
206 uninfected, HIV-only, *Mtb*-only, and *Mtb*/HIV-coinfected. We first annotated cell types in the scRNA-seq

207 data using the Azimuth annotation database at the finest annotation level and then transferred these labels
208 to our spatial transcriptome data during deconvolution analysis in 'full mode'. Given that Visium spots may
209 span up to 6 individual cells, we opted to run deconvolution in 'full mode', as it allows identification of any
210 number of cells existing in each pixel. Consistent with CD4 gene expression in the tissues, cell type weights
211 for the $CD4^+$ T cells also revealed the highest abundance of $CD4^+$ T cells in the *Mtb*-infected mice, with
212 reduced abundance in the HIV-infected and coinfected mice (**Figure 1D**). In line with prior reports, $CD4^+$
213 T cell abundance was lower in coinfected mice compared to those with HIV-only infection[25] (**Figure 1D**).
214 Unexpectedly, the abundance of nonclassical monocytes was lower in all infection groups compared to
215 uninfected control (**Figure 1D**). NK cell abundance was lower in the coinfection group than in the other
216 three groups, and the NK cell abundance was the highest in the lungs with *Mtb* single infection (**Figure**
217 **1D**), corroborating earlier findings of reduced NK cell infiltration during coinfection relative to *Mtb*-only
218 infection[25]. The distributions of the weights of myeloid lineage cells, such as alveolar macrophages, $CCL3^+$
219 alveolar macrophages, classical monocytes, monocyte-derived macrophages, and interstitial macrophages,
220 were similar across all groups, suggesting that infection status has minimal or no effect on the infiltration
221 of these cells (**Figure S2A**). However, B cells exhibited reduced abundance in HIV-infected and coinfected
222 groups compared to uninfected and *Mtb*-only infected controls (**Figure S2B**). Taken together, these results
223 suggest that lung tissue infiltration of various immune cell types depends on the type of infection.

224 **Validation of lung immune cell infiltration patterns using IMC**

225 To validate the results of spatial transcriptome data, we performed IMC on lung tissues from one
226 mouse with *Mtb*-only infection and one with *Mtb*/HIV coinfection. IMC is a multiplexed imaging technique
227 that enables comprehensive and accurate analysis at the single-cell level with spatial resolution using metal
228 tagged antibodies. IMC confirmed a reduced abundance of CD4+ T cells in coinfected lungs compared to
229 *Mtb*-only infection (**Figure 2A**), supporting the findings of spatial transcriptome data. Similarly, the
230 frequency of CD8+ T cells (**Figure 2B**) and B cells (**Figure S3A**) were less in coinfection group compared
231 to *Mtb*-only infection. While robust deconvolution of spatial data was limited due to the underrepresentation

232 of certain cell types in the reference dataset, IMC enabled analysis of cell population not covered in the
233 spatial data deconvolution. Notably, granulocytes, which were not assessed in spatial transcriptomics
234 analysis due to their absence in the reference dataset used for deconvolution, showed a lower abundance in
235 coinfected lungs compared to *Mtb*-only infection (**Figure 2C**). Similarly, dendritic cells also showed lower
236 abundance in coinfection compared to *Mtb*-only infection (**Figure S3B**). Collectively, both spatial
237 transcriptomics and IMC consistently demonstrated reduced infiltration of major immune cell types in
238 confected lungs compared to *Mtb*-only infection, suggesting a weakened immune response against *Mtb* in
239 the context of HIV infection.

240 **Lung immune cell infiltration patterns differ depending on infection status and the local histological**
241 **milieu**

242 To understand the distinct patterns of immune cell infiltration into the lungs, we clustered the
243 Visium spots across all 4 infection states together using uniform manifold approximation and projection
244 (UMAP) based on 50 principal components at a resolution of 0.9. This analysis identified a total of 14
245 clusters across 4 samples: no infection (12), HIV (11), *Mtb* (12), or coinfection (12) (**Figure 3A, S4A**).
246 Clusters 0-11 were present in all 4 samples, whereas Cluster 12 was absent in HIV and coinfection samples.
247 Intriguingly, Cluster 13 was detected exclusively in the coinfection group (**Figure S4A**).

248 The UMAP analysis (**Figure 3A**) revealed a broad separation of all 14 clusters into three distinct
249 groups (**Figure 3A**). The majority of the clusters, including Clusters 0-3, 5-8, 10, 11 and 13 (11 total
250 clusters), were placed together on the right of the UMAP projection as a single large group (**Figure 3B**).
251 These spots corresponded to the alveolar/interstitial compartment of the lung across all 4 infection
252 categories (**Figure 3B, S4B**). Therefore, we combined these 11 clusters into one large cluster, namely, the
253 'alveolar/interstitial' cluster, for further analysis. Clusters 4 and 12, positioned separately and distant from
254 the alveolar/interstitial cluster on the UMAP projection (**Figure 3C**; represented in green and blue,
255 respectively), were closer to each other than to cluster 9 on UMAP projection, suggesting similarities
256 between cluster 4 and 12. (**Figure S4C**; represented in green and blue, respectively). Therefore, we

257 combined Clusters 4 and 12 into one cluster called 'airway_1' (**Figure S4C**; represented in red) for
258 preliminary analysis. Similarly, Cluster 9, another distinct cluster far away from the rest on the UMAP, also
259 harbored spots representing airways across all four groups. It was then renamed 'airway_2' for further
260 analysis. Despite both airway-1 and airway_2 clusters representing airways, they were not combined due
261 to their distinct separation on the UMAP. Interestingly, cluster separation was driven by tissue location and
262 histological features rather than infection status. These findings suggest that immune infiltration is more
263 strongly influenced by histological features than by infection status in this study.

264 To investigate the differences in immune infiltration patterns across histological clusters, we
265 analyzed cell type weights obtained from the deconvolution analysis described in Figure 1. Monocyte-
266 derived macrophages were more abundant in the airway-1 cluster compared to other groups (**Figure S4D**).
267 Notably, the airway-2 cluster was enriched with $CCL3^{+}$ alveolar macrophages, which are known for
268 effective bacteria and antigen phagocytosis (**Figure 3D**)[26]. In contrast, alveolar macrophages with lower
269 CCL3 expression were slightly more abundant in the airway_1 cluster (**Figure 3D**). Additionally,
270 nonclassical monocytes were less abundant in the airway_2 cluster and alveolar/interstitium clusters
271 compared to the airway_1 cluster (**Figure 3D**).

272 The alveolar/interstitial cluster was enriched with $CD8^{+}$ T cells and classical monocytes, whereas
273 the number of type 2 dendritic cells was lower (**Figure 3D**). The abundance of B cells, mast cells and type
274 1 dendritic cells was similar across the three clusters (**Figure S4E**). These results suggest that different
275 histological regions may harbor distinct immune cell types. However, it remains unclear whether this
276 differential abundance contributes to distinct immune responses.

277 **Airways of *Mtb* infection exhibit different immune cell patterns compared to HIV and coinfection**

278 In uninfected mice, all airways exclusively belonged to cluster 4. In contrast, mice with HIV and
279 coinfection have both cluster 4 and cluster 9, but not cluster 12. The cluster 12 was unique to *Mtb*-only
280 infected mice. Given that cluster 4 is present in uninfected mice, and clusters 9 and 12 appear to be stratified

281 based on infection type, we compared the transcriptomic signatures in cluster 12 and 9. As our spatial assay
282 was specific to human transcriptome, the robust segregation of two different airway clusters and their
283 stratification by infection type suggests that the airways in *Mtb*-only infected group may harbor a unique
284 immune cell population compared to those with HIV or coinfection. To investigate this further, we
285 performed Gene Set Enrichment Analysis (GSEA) using human immunologic gene sets (C8, n=886) to map
286 the immune response signatures associated with both clusters. We sought to decipher how HIV infection
287 affects airway immune cell population and differs from *Mtb* infection. GSEA analysis on clusters 9 and 12
288 revealed a reduced abundance of proinflammatory M1 macrophages in HIV infection (**Figure 4A**), which
289 produce TNF-alpha and IL-12 and exhibit anti-mycobacterial activity through nitric oxide production and
290 autophagy. Highlighting the disruption of immune response against *Mtb* in coinfection, GSEA revealed the
291 diminishing of M1 macrophages in cluster 9 which represents airways from HIV and coinfection. This
292 depletion of M1 macrophages would potentially facilitate the progression of *Mtb* infection. GSEA also
293 revealed lower abundance of neutrophils (**Figure 4B**) and classical monocytes (**Figure 4C**), alongside
294 increased frequency of NK cells (**Figure 4D**), innate lymphoid cells type 2 (**Figure 4E**), and nonclassical
295 monocytes (**Figure 4F**). Taken together, these results indicate that immune cell populations at the airway
296 interfaces may vary across disease type and HIV infection may disrupt the immune cell infiltration patterns
297 that aid the survival of TB pathogen.

298 **Cellular organization and composition of lymphoid cell aggregates markedly differ from those of**
299 **typical mature tuberculosis granulomas**

300 Several previous studies have investigated the cellular architecture of mature tuberculosis
301 granulomas[12,27-29]. A granuloma may appear as a tiny lymphoid cell aggregate at the initial stages and
302 progress into a nonnecrotic or central necrotic mature granuloma. However, our understanding of the
303 cellular architecture of lymphoid cell aggregates remains limited compared to that of mature granulomas.
304 Hematoxylin (H&E) staining identified a lymphoid aggregate in the region of tissue from coinfected mice
305 subjected to spatial transcriptome profiling. Focusing exclusively on this region, we investigated two key

306 questions: 1) whether the cellular architecture of lymphoid aggregates resembles or differs from that of
307 mature granulomas, and 2) whether the lymphoid aggregates present any transcriptomic changes
308 characteristic of mature granulomas.

309 Remarkably, we observed that spots belonging to Cluster 13, the only UMAP cluster that was
310 exclusively detected in coinfection, spanned the entire lymphoid cell aggregate in this sample, indicating a
311 unique transcription profile distinct from other tissues across all 4 infection groups (**Figure 5A**). This
312 lymphoid aggregate, located in the interstitial region adjacent to a large airway, appears to have densely
313 infiltrated lymphoid cells on H&E staining (**Figure 5B**). On UMAP, Cluster 13 co-localizes with other
314 interstitial region clusters but remains distinctly separate from them (**Figure 5C**).

315 Necrotic granulomas are structured around the central core of necrotic cell debris in which many
316 bacteria are concentrated. This necrotic core is surrounded by layers primarily composed of macrophages[2],
317 including epithelioid macrophages, interspersed with classical alveolar macrophages, monocyte-derived
318 macrophages, lipid-laden foamy macrophages, and giant cells[2]. A variety of other immune cell types are
319 observed at the periphery and within the epithelioid layers of the granuloma. Non-necrotic granulomas have
320 similar structural arrangements except that they do not have necrotic cores[2]. However, the cellular
321 architecture and dynamics of these lymphoid aggregates are poorly understood.

322 To decipher the cell type abundances in the Visium spots spanning the lymphoid cell aggregate, we
323 extracted cell type frequency predictions obtained from RCTD deconvolution analysis. We labeled spots
324 spanning the lymphoid cell aggregate as inner/core regions, edges and peripheries, beginning from the
325 center to the outer region (**Figure 5D**). To compare the abundance of different immune cells predicted using
326 deconvolution analysis, we plotted a heatmap with hierarchical clustering of genes and spots (**Figure 5E**).
327 Interestingly, we observed that the spotwise clustering, as depicted in the column dendrogram, effectively
328 distinguished the peripheral spots from the inner and edge spots, indicating location-based stratification of
329 cell distribution. Unlike mature tuberculosis granulomas, where B cells predominantly present in the
330 periphery and are absent or scarce in the core, lymphoid aggregates exhibited a high abundance of B cells

331 in the inner/core region (**Figure 5E**). This was supported by elevated expression of mature B-cell markers,
332 such as CD19 (**Figure 5F**), CD20 (MS4A1) (**Figure S5A**), and IgM (IGHM) (**Figure S5B**). Plasmacytoid
333 dendritic cells (pDCs) were also highly enriched in the core and edge regions, as shown in the heatmap
334 (**Figure 5E**), consistent with high expression of pDC markers such as CD123 (IL3RA) (**Figure 5G**) and
335 CD303 (CLEC4C) (**Figure S5C**). Similarly, lymphoid aggregates abundantly harbor nonclassical
336 monocytes (**Figure 5E**), marked by elevated levels of CD97 (ADGRE5), P2RX1, and Siglec10[30]. As
337 expected, we observed a high abundance of CD97 (ADGRE5) (**Figure S5D**), P2RX1 (**Figure S5E**), and
338 Siglec10 (**Figure S5F**) in the core or edge of the lymphoid aggregate, with reduced abundance in the
339 periphery. Additionally, we also observed enrichment of plasma cells, DC2s, CD4+ T cells and nonclassical
340 monocytes in the core of the lesion (**Figure 5E**). In contrast, NK cells, mast cells, macrophages, CD8+ T
341 cells, DC1 cells, and classical monocytes were predominantly found in the periphery (**Figure 5E**).

342 Taken together, these results suggest that lymphoid cell aggregates may not essentially originate
343 with macrophages at their core. We hypothesize that granuloma architecture evolves over time, developing
344 into a macrophage-laden core surrounded by a lymphocyte-abundant periphery.

345 **Lymphoid cell aggregates displayed gene expression profiles typical of granulomas**

346 Given that lymphoid cell aggregates do not show a cellular architecture typical of a mature
347 granuloma, we assessed whether this lesion exhibited any transcriptomic changes associated with mature
348 granulomas. We examined the expression of genes that are part of gene sets related to granulomas using the
349 Molecular Signatures Database (MSigDB). We analyzed the HP_GRANULOMA gene set, which includes
350 ACP5, CYBB, CYBC1, DNASE2, DOCK2, IRF8, NF1, and PIK3CG. The lymphoid aggregate region
351 showed higher aggregated expression of these genes compared to other lung tissues (**Figure 6A**), with
352 individual genes also exhibiting elevated expression in this region (**Figure S6A**). Similarly, another gene
353 set, HP_ GRANULOMATOSIS, consisting of ASAH1, CTLA4, CYBA, CYBB, HLA-DPA1, HLA-DPB1,
354 NCF1, NCF2, PRTN3, and PTPN22, also exhibited increased expression in lymphoid aggregates compared
355 to the surrounding tissue (**Figure 6A, S6A, S7A**). These results suggest that gene expression changes

356 characteristic of mature granulomas emerge early during granuloma development from the lymphoid
357 aggregate.

358 Encouraged by these results, to elucidate the molecular changes occurring in the early stages of
359 granuloma development, we performed pathway analysis to identify signaling pathways enriched in the
360 lymphoid cell aggregate region. We performed differential expression analysis using the Seurat 'find-
361 markers' function to identify genes that were up- or downregulated in Cluster 13. Applying a log2FC cutoff
362 of 2 and an adjusted p value of 0.05, we identified 383 upregulated and 20 downregulated genes. Pathway
363 analysis was performed independently for both the up- and downregulated genes, revealing significant
364 enrichment of pathways related to immune response to viral, *Mtb*, and bacterial infections, as well as B-cell
365 and NK cell activity, cytokine signaling, glucose metabolism, oxidative phosphorylation, ROS generation,
366 interferon signaling, and the activation of several interferon regulatory factor (IRF) transcription factors in
367 genes upregulated in the lymphoid cell aggregate (**Figure 6B, Supplementary Table 1**). Interestingly,
368 oxidative phosphorylation and ROS generation are crucial for pathogen clearance within granulomas[31].
369 Transcriptional targets of several interferon regulatory factors (IRF5, IRF7, and IRF9) were enriched in
370 upregulated genes (**Figure 6B-C, Supplementary Table 1**). Additionally, type I interferon signaling
371 promotes *Mtb* infection by facilitating the release of neutrophil extracellular traps[32] and suppressing
372 interferon gamma and interleukin 1α/β signaling[33].

373 Intriguingly, similar analysis of downregulated genes revealed enrichment of multiple pathways
374 related to downregulation of inhibitory SMAD expression in lymphoid cell aggregates, suggesting potential
375 activation of TGFβ signaling (**Figure 6D**, **Supplementary Table 2**). This finding was corroborated by
376 decreased expression of SMAD6, which inhibits TGFβ signaling, alongside upregulation of TGFβ signaling
377 ligands, namely, TGFβ1/2, in the same tissue region, suggesting activated TGFβ signaling (**Figure 6E**).
378 Taken together, these results suggest that lymphoid cell aggregates present several granuloma-like
379 characteristics prior to evolving into mature granulomas.

380 **IRF7 and TGFβ signaling are active in T cells and macrophages.**
381 To determine the immune cell types that harbor active IRF7 and TGFβ signaling in the lungs, we
382 performed immunofluorescence staining on lung sections from mice infected with *Mtb* alone or coinfected
383 with *Mtb* and HIV. We used cell-specific markers along with IRF7 and TGFβ antibodies to assess whether
384 these signaling molecules colocalize with immune cells. Given that granulomas are predominantly
385 composed of macrophages, and HIV targets T cells, we examined these cell types for active IRF7 and TGFβ
386 signaling. Interestingly, expression levels of macrophage marker CD68 were decreased in *Mtb*/HIV-
387 coinfected mice compared to those infected with *Mtb* alone, suggesting that HIV infection may impair
388 macrophage recruitment and survival in the lungs, consistent with findings by Lepard et al., 2022[14] (Figure
389 7A). Similarly, the signal levels of T cells marker CD3 were comparatively lower in the coinfected group
390 relative to the *Mtb*-only group, likely reflecting the progressive depletion of $CD4^+$ T cells driven by HIV
391 infection (Figure 7B), consistent with findings from Berges et al., 2006[34]. In addition, we observed
392 consistent colocalization of intracellular markers IRF7 and TGFβ with these cells in both *Mtb*-only and
393 *Mtb*/HIV-coinfected lungs (Figure.7A&B). These results indicate that HIV coinfection reduces the overall
394 infiltration of macrophages and T cells in the lungs while these cells maintain active IRF7 and TGFβ
395 signaling.

396 **Discussion**

397 Novel spatial transcriptomic technologies provide a powerful tool to assess molecular and
398 immunological changes in situ in various tissues. This approach provides deeper insights into the host
399 response to infection, and the disease development or resistance[35,36]. In this study, we employed these
400 technologies to evaluate early molecular changes induced by HIV, *Mtb*, and their coinfection in humanized
401 mouse lung tissues. Although the lung is the main target organ of *Mtb*, it is also profoundly impacted by
402 HIV-induced generalized immunosuppression[9] due to massive depletion of the $CD4^+$ T cell population[8,9].
403 Following *Mtb* single infection, increased CD4+ T cell migration to affected sites aids in pathogen control[4].
404 Moreover, severe local depletion of this CD4+ T cell subset in HIV-infected hu-mice (with or without *Mtb*

405 coinfection) is a hallmark of HIV that has been previously reported[8] and observed in the present work. The
406 approach used in the present study also revealed alterations in less-studied populations, notably nonclassical
407 monocytes and NK cells. Intriguingly, while HIV and *Mtb* single infection increased NK cell populations
408 compared to uninfected controls, coinfection had the opposite effect. This pattern aligns with reported
409 changes in certain phenotypes of NK cells in HIV/*Mtb*-coinfected patients, suggesting that alterations in
410 this cell subset may vary in accordance with the phenotypes present in the individual subject[37].

411 A considerable portion of the differences evidenced in the cell populations presented within the
412 tissue corresponded not only to infection but also to distinct histological regions, with bronchi and major
413 airways clearly distinguished from interstitial tissue. However, even within clustered airway regions, viral
414 and bacterial infections altered the phenotypical landscape. This is evidenced by the high presence of
415 alveolar macrophages expressing CCL3 in the airway regions from all the infected animals, in contrast with
416 the uninfected controls. CCL3 aids in alveolar macrophage activation and efforts to control bacterial and
417 viral pathogens[26,38]. Recent studies have also shown increased CCL3 levels in COVID-19 patients with
418 alveolar damage, underscoring the important role of these cells in pulmonary immunity[39].

419 The reduction in M1 macrophages, neutrophils, and classical monocytes in HIV and coinfected
420 airways likely creates a permissive environment for *Mtb* survival. This supports the hypothesis that HIV
421 coinfection disrupts immune cell infiltration patterns necessary for controlling *Mtb*, thereby exacerbating
422 TB pathogenesis. Conversely, the increased abundance of NK cells and innate lymphoid cells type 2 (ILC2)
423 in HIV and coinfected airways suggests a shift toward innate lymphoid-driven immunity. This shift may
424 reflect an attempt to compensate for the loss of adaptive immunity (e.g., $CD4^+$ T cell depletion) or contribute
425 to immunopathology, such as excessive tissue remodeling driven by ILC2.

426

427 The finding of a structurally organized and clearly differentiated cell cluster with a unique
428 transcriptomic profile in a sample from an *Mtb*/HIV-coinfected mouse provides insight into the early

429 phenotypical and signaling changes induced by this dual infection. Spatial analysis revealed the presence
430 of both lymphoid and myeloid cells in the lymphoid aggregates. Remarkably, despite HIV-induced
431 generalized $CD4^+$ T cell depletion in the tissue, CD4+ T cells was found within the aggregate, primarily in
432 the inner region, alongside B cells and plasmacytoid DCs. Notably, unlike mature granulomas, which
433 typically feature a necrotic core surrounded by macrophages and epithelioid cells with lymphocytes in the
434 outer layer[2,3,7], the lymphoid aggregate in the *Mtb*/HIV-coinfected tissue lacked necrosis, with monocytic
435 cells positioned in the outer layer. This is likely because this cell aggregate is in the early stages of forming
436 a granulomatous structure, and the time after infection has not yet been sufficient to generate necrosis. This
437 observation is consistent with previous findings in a murine *Mtb* model, where inflammatory cell
438 aggregates, mainly adjacent to the circulation or bronchi, was detected as early as 2 weeks post-infection,
439 with the first necrotic changes detected approximately one month after infection[27,40]. Moreover, our results
440 show that the transcriptomic alterations found in this nascent granuloma-like structure mirror those reported
441 for mature granulomas, reinforcing the notion that the lymphoid aggregate found in this sample is in the
442 early stages of granuloma development.

443 The process of granuloma establishment involves precise modulation of the interferon pathway,
444 mainly through the upregulation of multiple IRFs, as shown in the cells present in this granuloma-like
445 structure. Some of the IRF genes that are upregulated in the lymphoid aggregate in this study have been
446 previously reported to be crucial for granuloma formation and maintenance, as evidenced by IRF8-deficient
447 mice, which fail to form these structures and control *Mtb* growth after infection[41]. However, the increased
448 transcription of different IRF genes suggests that the IFN response is regulated via multiple mechanisms,
449 including cell differentiation and innate immunity. This likely stems from the initial induction of type-I
450 IFNs and activation of the IFN pathway and IFN-stimulated genes (ISGs) after infection. However, the
451 relevance of this multifaceted IFN modulation in more advanced stages of structural remodeling remains
452 to be elucidated. While some studies suggest that mature granulomas (after 9 weeks post-infection) do not

453 show upregulation of these pathways, others report increased IRF transcription in these structures,
454 particularly in nonimmune cell types (fibroblasts)[6,42].

455 Consequently, the activation of the immune response by the IFN pathway leads to increased energy
456 requirements in the immune cells present in the lymphoid aggregate, as exemplified by the upregulation of
457 oxidative phosphorylation-related genes. This metabolic shift has been a well-documented consequence of
458 HIV, *Mtb*, and *Mtb*/HIV coinfection[43-45]. Our results show that the generalized metabolic changes induced
459 by *Mtb*/HIV coinfection also occur locally in the affected tissues and, particularly in the affected areas,
460 starting at an early stage of infection.

461 Our findings indicate that, unlike the regulation of the IFN pathway, TGFβ regulation is absent.
462 TGFβ inhibition of *Mtb*-specific $CD4^+$ T cells contributes to the maintenance of *Mtb* within mature
463 granuloma structures in rhesus macaque and mouse models[46]. Additionally, TGFβ and its associated
464 pathways have also been proposed as determinants of myeloid cell differentiation in TB granulomas[47],
465 whereas computational modeling suggests enhanced bacterial clearance in the absence of TGFβ[48]. The
466 concurrent reduction in macrophages and T cells, coupled with active IRF7 and TGFβ signaling, suggests
467 a complex interplay where HIV coinfection may skew and disrupt immune responses. Investigating whether
468 IRF7 drives pro-inflammatory responses or TGFβ promotes immunosuppression could provide insights into
469 disease progression.

470

471 **Conclusions**

472 The modulation of the immune response by pathogens is an important determinant of the outcome
473 of infection, ranging from generalized immunosuppression, as seen with HIV, to more nuanced modulation
474 of the immune response induced by *Mtb*. This study examines the effects of these pathogens, whether in
475 the context of single infection or coinfection, on lung tissue in a humanized NSG-SGM3-IL15 mouse model
476 at an early timepoint after inoculation. Our findings suggest that early infection triggers alterations in

477 cellular infiltration and structural remodeling of the tissue, mirroring the patterns observed in humans and
478 other animal models. These findings further validate the humanized NSG-SGM3-IL15 mouse strain as a
479 reliable animal model for studying HIV, *Mtb*, and *Mtb*/HIV coinfection. Nevertheless, future studies using
480 higher-resolution spatial transcriptomics will further elucidate the transcriptomic changes in lung immune
481 cell populations at the single-cell level, providing further detail into specific changes in different cell
482 populations, both in terms of phenotype and signaling. Such insights may pave the way for novel
483 intervention strategies that improve infection outcomes in patients infected with HIV and *Mtb* infections.

484

485 **Data sharing statement**

486 All data supporting the findings of this study are available in the manuscript. Raw and processed spatial
487 transcriptome data was deposited in the National Center for Biotechnology Information (NCBI) Gene
488 Expression Omnibus (GEO)and can be accessed at GSE303811. If there are any special requests or
489 questions for the data, please contact the corresponding author (G.Y.).

490 **Acknowledgments**

491 We thank the technical support from the Cancer Prevention and Research Institute of Texas (CPRIT
492 RP240610). We thank the Texas Advanced Computing Center (TACC) at The University of Texas at Austin
493 for providing computational resources that have contributed to the research results reported within this
494 paper. We'd like to thank Drs. Buka Samten and Amy Tvinnereim for their aid in *Mtb* infection of the
495 humanized mice.

496 **Funding:**

497 This work was supported by a NIH Common funds/National Institute of Allergy and Infectious Diseases
498 grant UG3AI150550, a National Institute of Allergy and Infectious Diseases grant R01AI184551, and a
499 National Heart, Lung, and Blood Institute grant R01HL125016 to GY.

500 **Contributions**

501 Sitaramaraju Adduri: Conceptualized the study, designed and performed the experiments, analyzed data,
502 edited figures, and wrote the manuscript.

503 Jose Alejandro Bohorquez: Conceptualized the study, designed and perform the experiments, analyzed data,
504 edited figures, and wrote the manuscript.

505 Rajesh Mani: Perform the experiments, analyzed data, edited figures, and wrote the manuscript.

506 Omoyeni Adejare: Perform the experiments.

507 Diego Rincon: Analyzed data.

508 Joshua K. Kleam: Perform the experiments.

Mounika Duggineni: Perform the experiments.

Andy Omeje: Perform the experiments.

Torry Tucker: Edited the manuscript, provided critical resources.

Nagarjun V Konduru: Designed the experiments, edited the manuscript.

Guohua Yi: Conceptualized and guided the study, secured the funding, designed the experiments, analyzed data, edited figures, and wrote, edited, and finalized the manuscript.

Competing interests

All the authors declare no competing interests.

Figure legends:

Figure 1. Cell type abundance variations between control, HIV, *Mtb* and coinfection mice as predicted by cell specific marker analysis and cell type deconvolution analysis. A) The experimental protocol. The number of mice was four per group. **B&C)** Expression levels of CD45 (PTPRC) and CD4 genes were shown across the four groups. **D)** Cell type weights for each spot in the samples based on RCTD analysis were plotted for each infection type. X axis shows cell types of weights which are proportional to the cell type abundance in the tissue. The difference in cell weight distributions was computed using Kruskal Wallis test followed by Dunn's test for pairwise comparisons. P were adjusted for multiple hypothesis testing using Bonferroni correction method. Significance levels are indicated as $*P < .05$, $**P < .01$, $***P < .001$, and $****P < .0001$.

Figure 2: Spatial distribution map of CD4+ and CD8+ T cells, and granulocytes in the lungs from *Mtb* infection and coinfection mice. Ir-Intercalator was used to stain nucleus. 195Pt_ICSK2 was used for staining plasma membrane. 156Gd_CD4, 162Dy_CD8, and 160Gd_CD66b were used to detect CD4+ T cells **(A)**, CD8+ T cells **(B)**, and granulocytes **(C)**, respectively.

Figure 3. Identification clusters based on gene expression of all tissue spots from no infection, HIV, *Mtb*, and coinfection mice lungs using Seurat package. A) Clusters from all four samples projected on UMAP and color based on cluster identifier (left) and sample type (right). **B)** Alveolar/interstitium cluster (shown in blue), **C)** airway_1 (shown in blue/green) and airway-2 (shown in red) clusters on UMAP projection. **D)** Cell type weights obtained in RCTD deconvolution analysis were plotted for each cluster. Y axis shows cell type weights which are proportional to the cell type abundance in the corresponding cluster. The color key indicated the cluster identifier. The difference in cell weight distributions was computed using Kruskal Wallis test followed by Dunn's test for pairwise comparisons. P values were adjusted for multiple hypothesis testing using Bonferroni correction method. Significance levels are indicated as $*P < .05$, $**P < .01$, $***P < .001$, and $****P < .0001$.

Figure 4. Gene set enrichment analysis for identifying differences in immune cell types between cluster 9 compared to cluster 4 shown in figure 2C. The enrichment plots illustrate the enrichment of the corresponding gene set in the ranked list of genes based on comparison between Cluster 9 vs cluster 4. Gene set names for each enrichment plot were shown on the top. **A)** M1 macrophages, **B)** Neutrophils, **C)** S100A12 +ve classical monocytes, **D)** NK cells, **E)** type 2 Innate lymphoid cells, and **F)** nonclassical monocytes. The x-axis represents the rank of genes based on their differential expression, ordered from most upregulated to most downregulated. The y-axis shows the running enrichment score (ES), which quantifies the degree to which the gene set is overrepresented at the top or bottom of the ranked list. The green curve depicts the cumulative ES, with peaks indicating maximum enrichment. Vertical black lines mark the positions of genes within the gene set. The Normalized Enrichment Score (NES) reflects the enrichment score normalized for gene set size and dataset variability, with positive/negative values indicating enrichment in upregulated/downregulated genes in cluster 9, respectively. Msigdb identifier of the gene set corresponding to each enrichment plot was shown in parenthesis.

Figure 5: Characterization of the unique cluster (cluster 13) detected in HIV/*Mtb* coinfection mouse lung. A) Spatial mapping of cluster 13 which was detected exclusively in coinfection lung. Clusters were identified on UMPA projection of all Visium spots passing quality control from all four infection groups combined. Spots representing cluster 13 were highlighted in blue. **B)** Hematoxylin staining of lung region matching with cluster 13 location in coinfection lung. This region contains a circular lymphoid aggregate

562 formed by dense lymphocyte infiltration located within the interstitial region and close to two airways. **C)**
563 UMAP projection of all Visium spots passing quality control from all four infection groups highlighting
564 the location of cluster 13. **D)** Projection of the Visium spots overlapping with lymphoid aggregate shown
565 in Figure 3B. The spots were labeled as core/inner region, edge, and periphery depending on the location
566 and were highlighted according to the label with different colors. **E)** Heatmap showing the cell type
567 abundances all the spots highlighted in Figure 3D. Columns show individual spots spanning the lymphoid
568 aggregate. The rows show the immune cells detected in the spots. Color intensities represent the
569 abundance of each cell in each spot. Row and column dendrograms represent the similarity between cell
570 abundances and individual spots, respectively, as computed using hierarchical clustering. **F)** Spatial map
571 of expression of CD19, a mature B cell marker within and around the lymphoid aggregate. Spot-wise
572 gene expression data was projected on hematoxylin staining image of the lung tissue. Color key
573 represents the level of transcript expression. **G)** Expression of CD123 (IL3RA), plasmacytoid markers in
574 the same region as described for Figure 5F.

575 **Figure 6: Gene expression changes and pathway analysis of lymphoid aggregate. A)** Aggregated gene
576 expression of granuloma and granulomatosis gene sets from MSigDB projected on hematoxylin stain of
577 lungs from coinfection mice. Spot-wise gene expression aggregate was projected on lymphoid cell
578 aggregate and its surround tissue. Color key represents aggregate of expression values of all the genes in
579 the granuloma gene set (DOCK2, CYBC1, PIK3CG, CYBB, IRF8, NF1, DNASE2, and ACP5) and
580 granulomatosis gene set (DOCK2, CYBC1, PIK3CG, CYBB, IRF8, NF1, DNASE2, and ACP5). **B)** Top
581 20 pathways based on an adjusted p value identified in over representation analysis on gene upregulated
582 in cluster 13 spanning lymphoid cell aggregate in coinfection mice. Gene ratios were computed as the
583 percentage of total DEGs in the given pathway term. **C)** Expression levels of interferon regulatory factors
584 enriched among upregulated genes in lymphoid cell aggregate were projected individually on lymphoid
585 cell aggregate and its surround tissue. **D)** Top 20 pathways identified in over representation analysis on
586 gene down regulated in cluster 13 as shown like figure 4B. **E)** Down regulation of SMAD6, an inhibitory
587 SMAD and upregulation of TGFB1/2 in lymphoid cell aggregate. Gene expression levels quantified in
588 spatial transcriptomics analysis were projected on hematoxylin-stained tissue section. A, C, E) Color key
589 represents aggregate/individual gene expression values in log2 scale.

590 **Figure 7. Dynamics of macrophages and T cells in the lungs of mice infected with *Mtb* or *Mtb*/HIV**
591 **coinfection**. Immunofluorescence staining was performed on FFPE lung sections from mice infected with
592 *Mtb* alone or coinfected with *Mtb* and HIV to examine immune cell infiltration and the colocalization of
593 intracellular signaling molecules IRF-7 and TGF-β. **A)** Sections were surface-stained for human
594 macrophage marker CD68, along with intracellular markers IRF-7 and TGF-β. **B)** Sections were surface-
595 stained for human T-cell marker CD3, along with intracellular IRF-7 and TGF-β. DAPI-supplemented
596 mounting medium was used for nuclear staining. Representative images were acquired at 20×
597 magnification using a Zeiss LSM-500 confocal microscope. Scale bars: 100 µm.

598

599 **Figures**

600 **Figure 1**

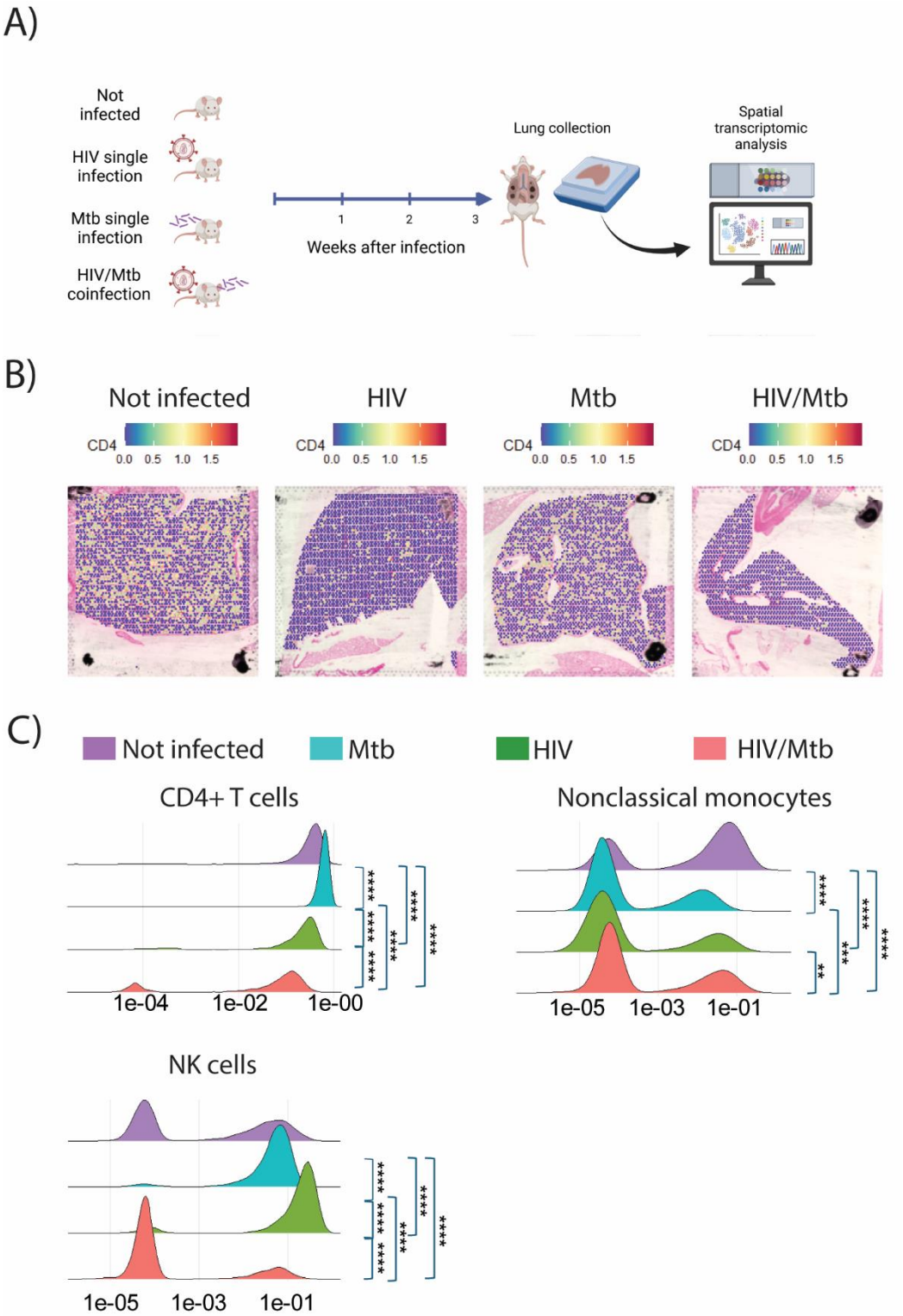

601

602

Figure 2

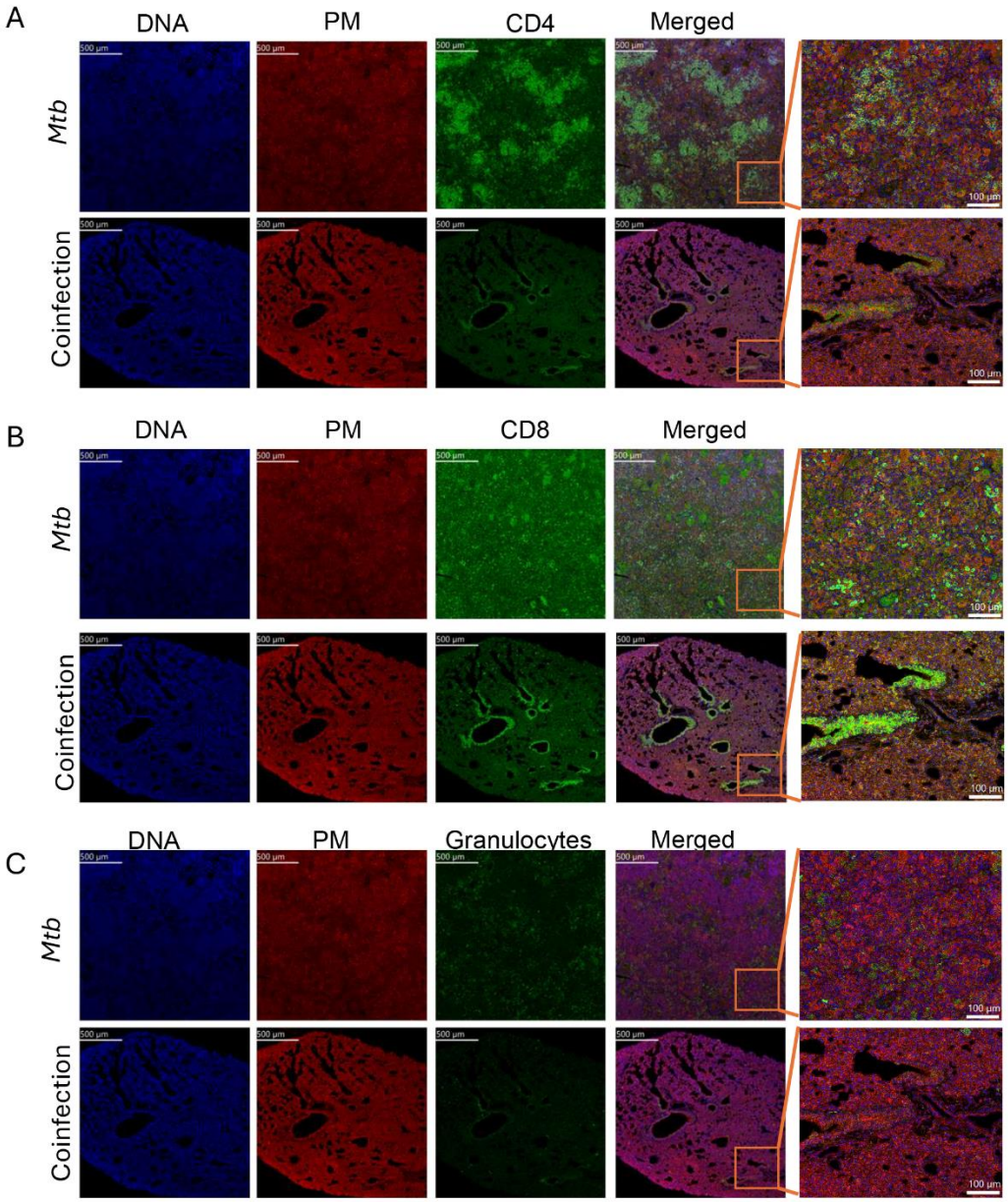

603

604

Figure 3

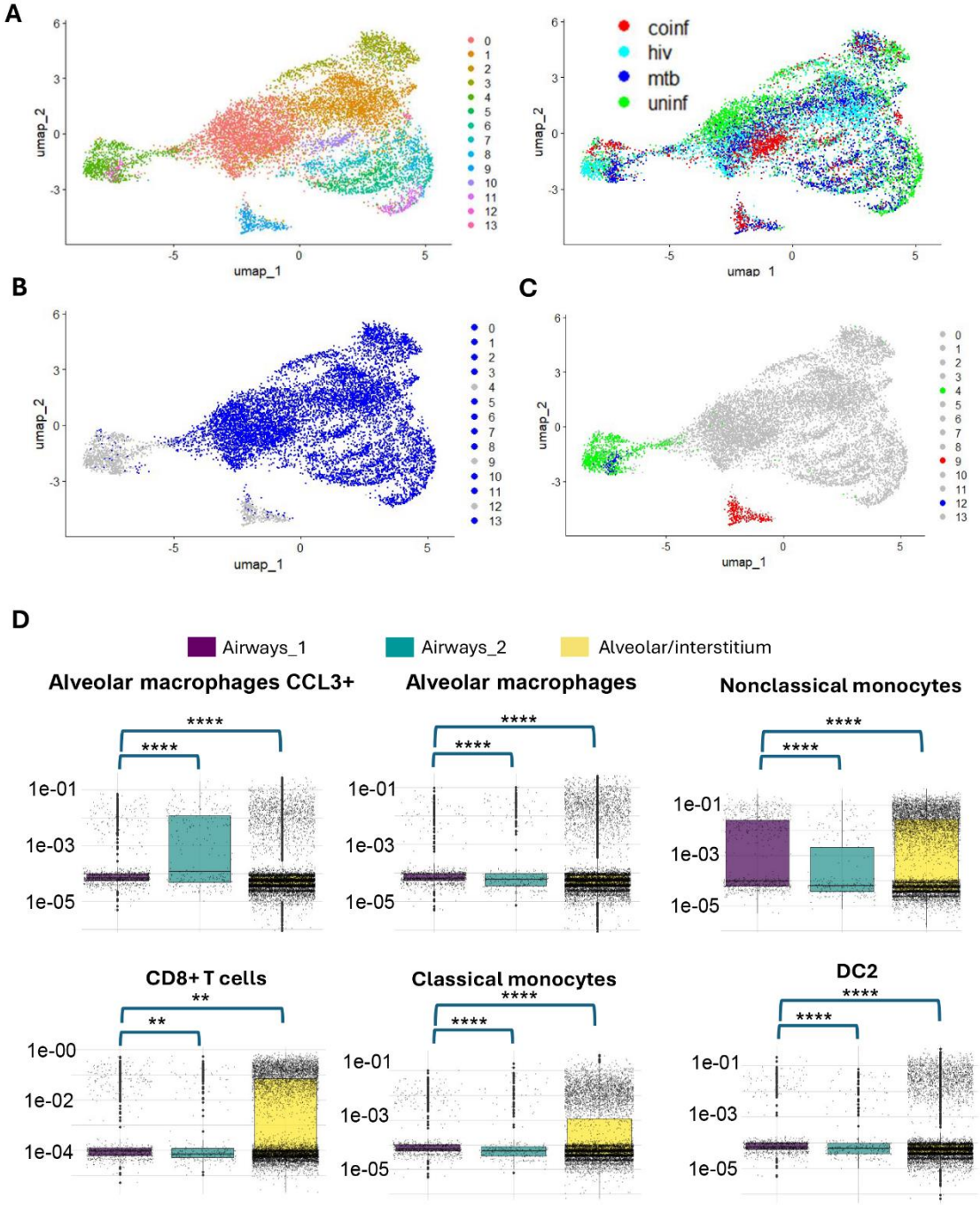

605

606

Figure 4

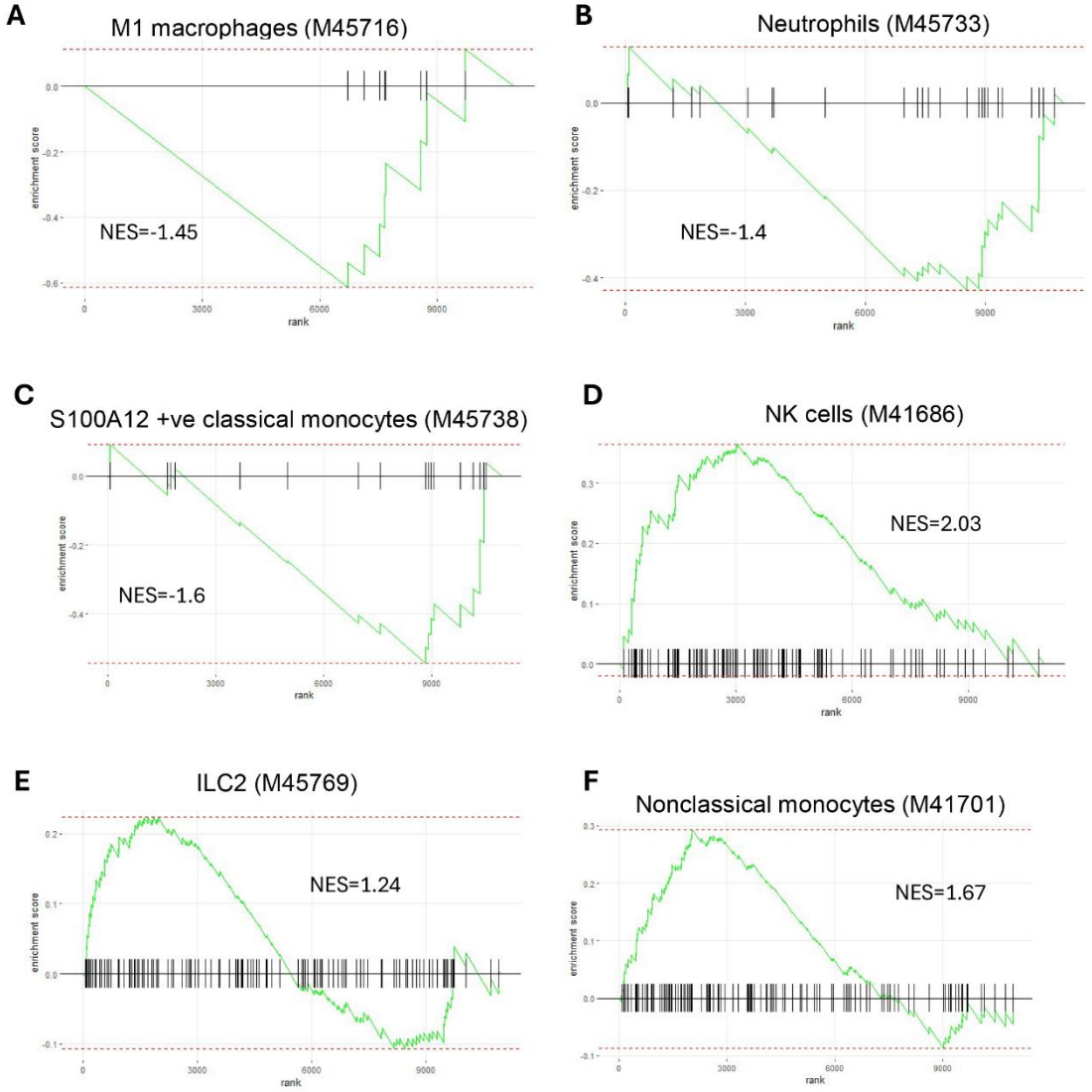

607

608

Figure 5

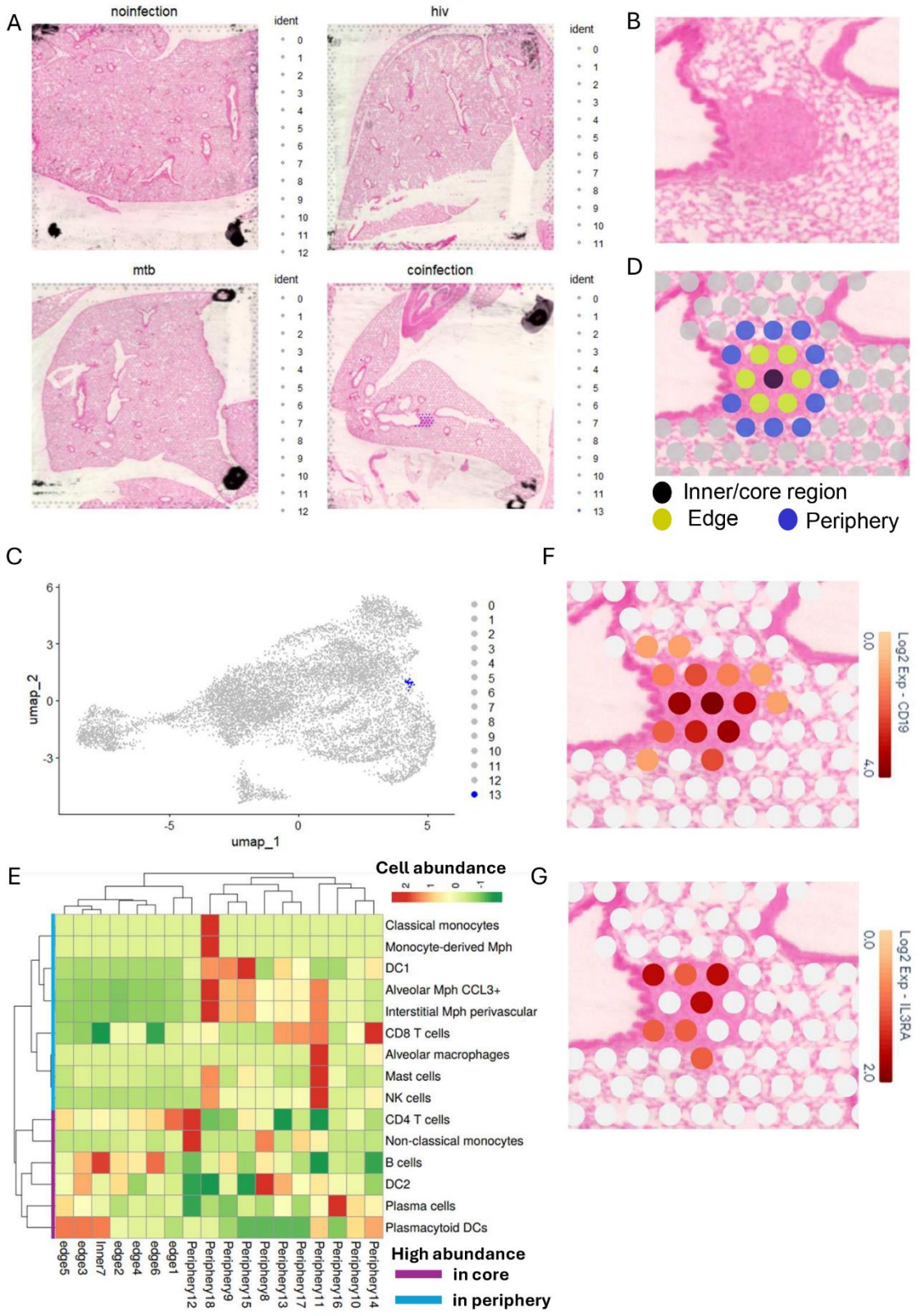
A
noinfection
hiv
mtb
coinfection
ident
B
D
Inner/core region
Edge
Periphery
C
umap_1
umap_2
F
Log2 Exp - CD19
G
Log2 Exp - IL3RA
E
Cell abundance
Classical monocytes
Monocyte-derived Mph
DC1
Alveolar Mph CCL3+
Interstitial Mph perivascular
CD8 T cells
Alveolar macrophages
Mast cells
NK cells
CD4 T cells
Non-classical monocytes
B cells
DC2
Plasma cells
Plasmacytoid DCs
High abundance
in core
in periphery

609

Figure 6

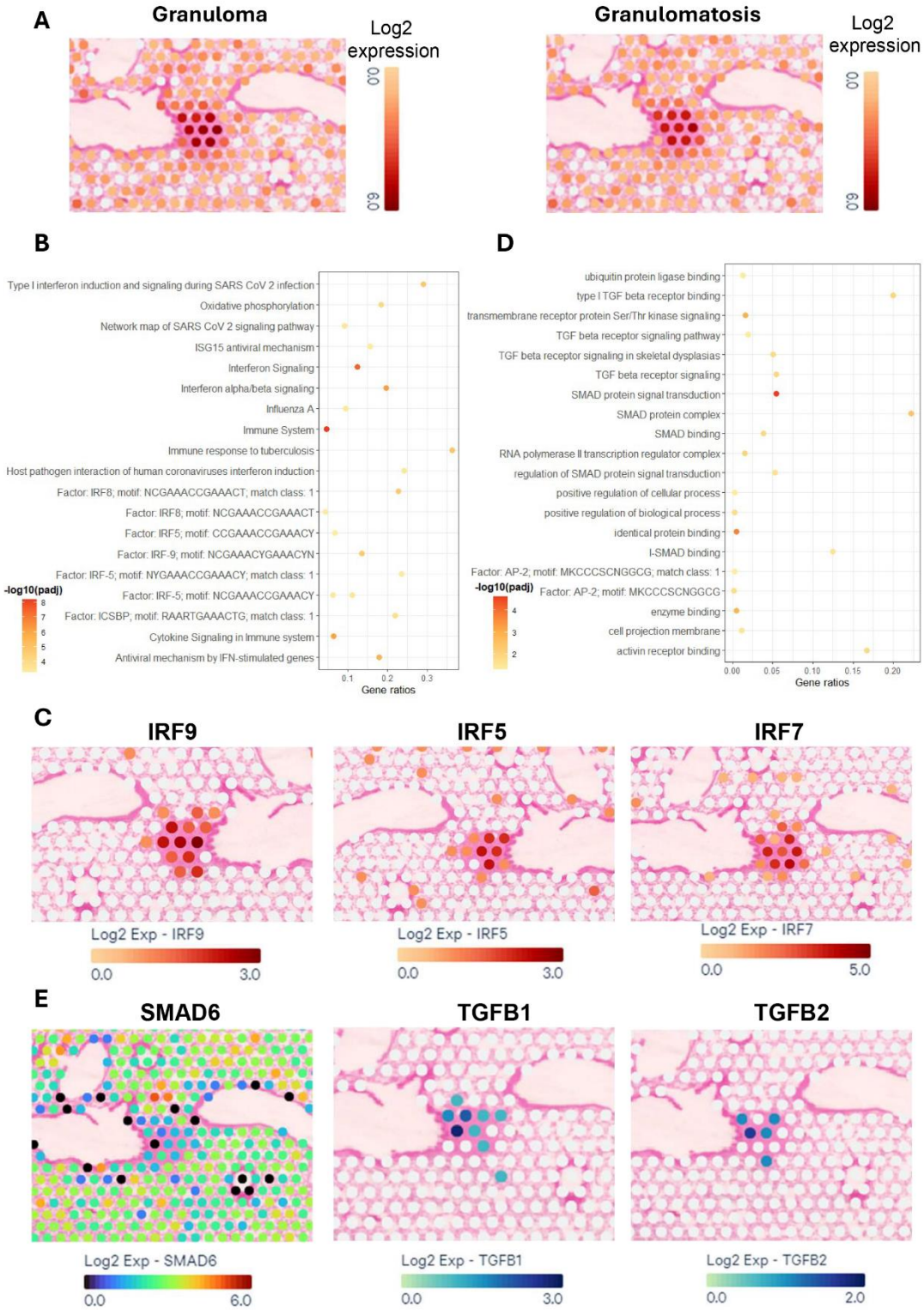
A
Granuloma
Log2 expression
0.0
6.0
Granulomatosis
Log2 expression
0.0
6.0
B
Type I interferon induction and signaling during SARS CoV 2 infection
Oxidative phosphorylation
Network map of SARS CoV 2 signaling pathway
ISG15 antiviral mechanism
Interferon Signaling
Interferon alpha/beta signaling
Influenza A
Immune System
Immune response to tuberculosis
Host pathogen interaction of human coronaviruses interferon induction
Factor: IRF8; motif: NCGAAACCGAAACT; match class: 1
Factor: IRF8; motif: NCGAAACCGAAACT
Factor: IRF5; motif: CCGAAACCGAAACY
Factor: IRF-9; motif: NCGAAACYGAAACYN
Factor: IRF-5; motif: NYGAAACCGAAACY; match class: 1
Factor: IRF-5; motif: NCGAAACCGAAACY
Factor: ICSBP; motif: RAARTGAAACTG; match class: 1
Cytokine Signaling in Immune system
Antiviral mechanism by IFN-stimulated genes
-log10(padj)
8
7
6
5
4
0.1
0.2
0.3
Gene ratios
D
ubiquitin protein ligase binding
type I TGF beta receptor binding
transmembrane receptor protein Ser/Thr kinase signaling
TGF beta receptor signaling pathway
TGF beta receptor signaling in skeletal dysplasias
TGF beta receptor signaling
SMAD protein signal transduction
SMAD protein complex
SMAD binding
RNA polymerase II transcription regulator complex
regulation of SMAD protein signal transduction
positive regulation of cellular process
positive regulation of biological process
identical protein binding
I-SMAD binding
Factor: AP-2; motif: MKCCCSCNGGCG; match class: 1
Factor: AP-2; motif: MKCCCSCNGGCG
enzyme binding
cell projection membrane
activin receptor binding
-log10(padj)
4
3
2
0.00
0.05
0.10
0.15
0.20
Gene ratios
C
IRF9
IRF5
IRF7
Log2 Exp - IRF9
0.0
3.0
Log2 Exp - IRF5
0.0
3.0
Log2 Exp - IRF7
0.0
5.0
E
SMAD6
TGFB1
TGFB2
Log2 Exp - SMAD6
0.0
6.0
Log2 Exp - TGFB1
0.0
3.0
Log2 Exp - TGFB2
0.0
2.0

610

Figure 7

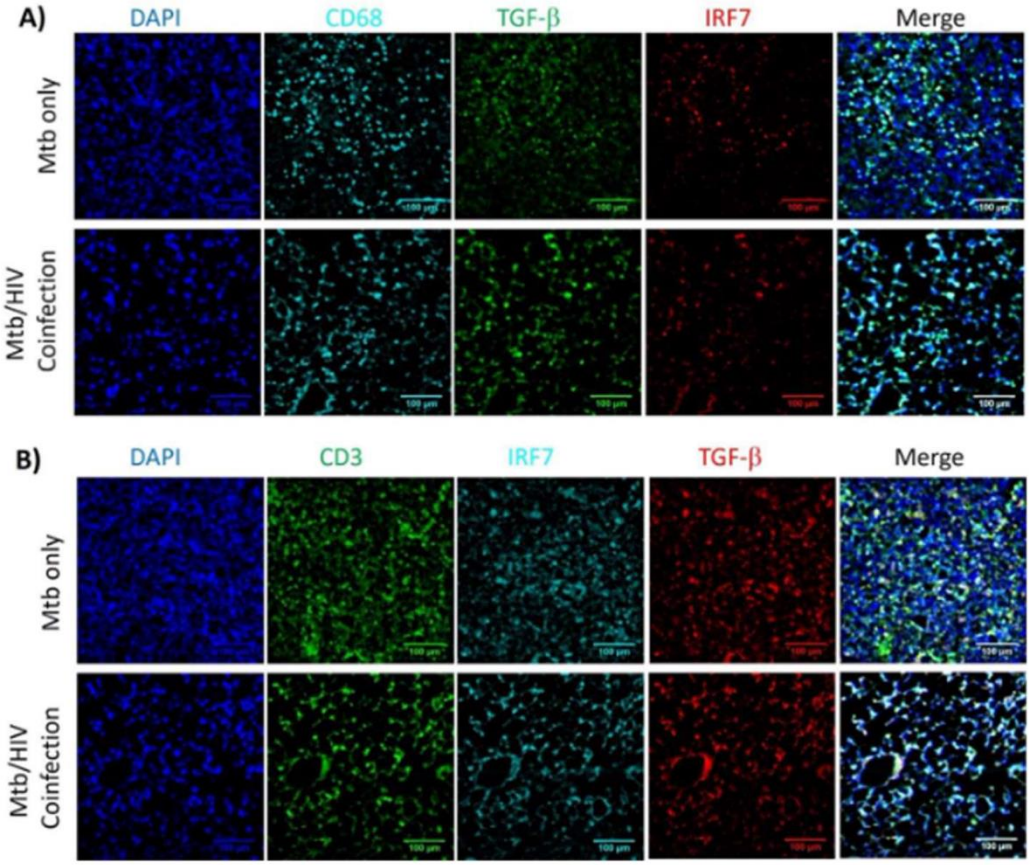
A)
DAPI
CD68
TGF-β
IRF7
Merge
Mtb only
Mtb/HIV Coinfection
B)
DAPI
CD3
IRF7
TGF-β
Merge
Mtb only
Mtb/HIV Coinfection

611

612 **References:**

613 1. WHO. Global Tuberculosis Report. Geneva, Switzerland: WHO, 2023.
614 2. Cronan MR. In the Thick of It: Formation of the Tuberculous Granuloma and Its Effects on Host
615 and Therapeutic Responses. *Frontiers in Immunology* 2022; **13**.
616 3. McCaffrey EF, Donato M, Keren L, et al. The immunoregulatory landscape of human
617 tuberculosis granulomas. *Nat Immunol* 2022; **23**(2): 318–29.
618 4. Bromley JD, Ganchua SKC, Nyquist SK, et al. CD4(+) T cells re-wire granuloma cellularity and
619 regulatory networks to promote immunomodulation following Mtb reinfection. *Immunity* 2024; **57**(10):
620 2380–98 e6.
621 5. Carow B, Hauling T, Qian X, Kramnik I, Nilsson M, Rottenberg ME. Spatial and temporal
622 localization of immune transcripts defines hallmarks and diversity in the tuberculosis granuloma. *Nat*
623 *Commun* 2019; **10**(1): 1823.
624 6. Krausgruber T, Redl A, Barreca D, et al. Single-cell and spatial transcriptomics reveal aberrant
625 lymphoid developmental programs driving granuloma formation. *Immunity* 2023; **56**(2): 289–306 e7.
626 7. Qiu X, Zhong P, Yue L, et al. Spatial transcriptomic sequencing reveals immune
627 microenvironment features of Mycobacterium tuberculosis granulomas in lung and omentum.
628 *Theranostics* 2024; **14**(16): 6185–201.
629 8. Foreman TW, Nelson CE, Kauffman KD, et al. CD4 T cells are rapidly depleted from
630 tuberculosis granulomas following acute SIV co-infection. *Cell Rep* 2022; **39**(9): 110896.
631 9. Kaushal D, Singh DK, Mehra S. Immune Responses in Lung Granulomas during Mtb/HIV Co-
632 Infection: Implications for Pathogenesis and Therapy. *Pathogens* 2023; **12**(9).
633 10. Azevedo-Pereira JM, Pires D, Calado M, et al. HIV/Mtb Co-Infection: From the Amplification of
634 Disease Pathogenesis to an "Emerging Syndemic". *Microorganisms 2023, Vol 11, Page 853* 2023–03–27;
635 **11**(4).
636 11. Bohorquez JA, Jagannath C, Xu H, Wang X, Yi G. T Cell Responses during Human
637 Immunodeficiency Virus/Mycobacterium tuberculosis Coinfection. *Vaccines (Basel)* 2024; **12**(8).
638 12. Sawyer AJ, Patrick E, Edwards J, et al. Spatial mapping reveals granuloma diversity and
639 histopathological superstructure in human tuberculosis. *J Exp Med* 2023; **220**(6).
640 13. Bohorquez JA, Adduri S, Ansari D, et al. A Novel Humanized Mouse Model for HIV and
641 Tuberculosis Co-infection Studies. *bioRxiv* 2024: 2024.03.05.583545.
642 14. Lepard M, Yang JX, Afkhami S, et al. Comparing Current and Next-Generation Humanized
643 Mouse Models for Advancing HIV and HIV/Mtb Co-Infection Studies. *Viruses* 2022; **14**(9).
644 15. Feng Y, Kong Y, Barnes PF, et al. Exposure to Cigarette Smoke Inhibits the Pulmonary T-Cell
645 Response to Influenza Virus andMycobacterium tuberculosis. *Infection and Immunity* 2011; **79**(1):
646 229–37.
647 16. Butler SL, Hansen MST, Bushman FD. A quantitative assay for HIV DNA integration in vivo.
648 *Nature Medicine* 2001; **7**(5): 631–4.
649 17. Morton J, Snider TA. Guidelines for collection and processing of lungs from aged mice for
650 histological studies. *Pathobiology of Aging & Age-related Diseases* 2017; **7**(1): 1313676.
651 18. Davenport ML, Sherrill TP, Blackwell TS, Edmonds MD. Perfusion and Inflation of the Mouse
652 Lung for Tumor Histology. *J Vis Exp* 2020; (162).
653 19. Hao Y, Stuart T, Kowalski MH, et al. Dictionary learning for integrative, multimodal and scalable
654 single-cell analysis. *Nat Biotechnol* 2024; **42**(2): 293–304.
655 20. Kolberg L, Raudvere U, Kuzmin I, Vilo J, Peterson H. gprofiler2 -- an R package for gene list
656 functional enrichment analysis and namespace conversion toolset g:Profiler. *F1000Res* 2020; **9**.
657 21. Cable DM, Murray E, Zou LS, et al. Robust decomposition of cell type mixtures in spatial
658 transcriptomics. *Nat Biotechnol* 2022; **40**(4): 517–26.
659 22. Wang L, Ma H, Wen Z, et al. Single-cell RNA-sequencing reveals heterogeneity and intercellular
660 crosstalk in human tuberculosis lung. *J Infect* 2023; **87**(5): 373–84.

661 23. Hao Y, Hao S, Andersen-Nissen E, et al. Integrated analysis of multimodal single-cell data. *Cell*
662 2021; **184**(13): 3573–87 e29.
663 24. Bohorquez JA, Adduri S, Ansari D, et al. A novel humanized mouse model for HIV and
664 tuberculosis co-infection studies. *Front Immunol* 2024; **15**: 1395018.
665 25. Xiao G, Huang W, Zhong Y, et al. Uncovering the Bronchoalveolar Single-Cell Landscape of
666 Patients With Pulmonary Tuberculosis With Human Immunodeficiency Virus Type 1 Coinfection. *J Infect*
667 *Dis* 2024; **230**(3): e524–e35.
668 26. Lindell DM, Standiford TJ, Mancuso P, Leshen ZJ, Huffnagle GB. Macrophage inflammatory
669 protein 1alpha/CCL3 is required for clearance of an acute Klebsiella pneumoniae pulmonary infection.
670 *Infect Immun* 2001; **69**(10): 6364–9.
671 27. Tsai MC, Chakravarty S, Zhu G, et al. Characterization of the tuberculous granuloma in murine
672 and human lungs: cellular composition and relative tissue oxygen tension. *Cell Microbiol* 2006; **8**(2):
673 218–32.
674 28. Marakalala MJ, Raju RM, Sharma K, et al. Inflammatory signaling in human tuberculosis
675 granulomas is spatially organized. *Nat Med* 2016; **22**(5): 531–8.
676 29. Kumar R, Kolloli A, Subbian S, Kaushal D, Shi L, Tyagi S. Imaging the Architecture of
677 Granulomas Induced by Mycobacterium tuberculosis Infection with Single-molecule Fluorescence In Situ
678 Hybridization. *J Immunol* 2024; **213**(4): 526–37.
679 30. Wong KL, Tai JJ, Wong WC, et al. Gene expression profiling reveals the defining features of the
680 classical, intermediate, and nonclassical human monocyte subsets. *Blood* 2011; **118**(5): e16–31.
681 31. Song E, Jaishankar GB, Saleh H, Jithpratuck W, Sahni R, Krishnaswamy G. Chronic
682 granulomatous disease: a review of the infectious and inflammatory complications. *Clin Mol Allergy*
683 2011; **9**(1): 10.
684 32. Chowdhury CS, Kinsella RL, McNehlan ME, et al. Type I IFN-mediated NET release promotes
685 Mycobacterium tuberculosis replication and is associated with granuloma caseation. *Cell Host Microbe*
686 2024; **32**(12): 2092–111 e7.
687 33. Donovan ML, Schultz TE, Duke TJ, Blumenthal A. Type I Interferons in the Pathogenesis of
688 Tuberculosis: Molecular Drivers and Immunological Consequences. *Front Immunol* 2017; **8**: 1633.
689 34. Berges BK, Wheat WH, Palmer BE, Connick E, Akkina R. HIV-1 infection and CD4 T cell
690 depletion in the humanized Rag2-/-gamma c-/- (RAG-hu) mouse model. *Retrovirology* 2006; **3**: 76.
691 35. Marx V. Method of the Year: spatially resolved transcriptomics. *Nat Methods* 2021; **18**(1): 9–14.
692 36. Williams CG, Lee HJ, Asatsuma T, Vento-Tormo R, Haque A. An introduction to spatial
693 transcriptomics for biomedical research. *Genome Med* 2022; **14**(1): 68.
694 37. Gao J, Huang X, Zhu Q, et al. Mtb/HIV co-infection immune microenvironment subpopulations
695 heterogeneity. *Int Immunopharmacol* 2024; **143**(Pt 1): 113341.
696 38. Sadee W, Cheeseman IH, Papp A, et al. Human alveolar macrophage response to Mycobacterium
697 tuberculosis: immune characteristics underlying large inter-individual variability. *Res Sq* 2023.
698 39. Garcia-Prieto CA, Musulen E, Davalos V, et al. Spatial transcriptomics unveils the *in situ* cellular
699 and molecular hallmarks of the lung in fatal COVID-19. *bioRxiv* 2024: 2024.07.03.601404.
700 40. Driver ER, Ryan GJ, Hoff DR, et al. Evaluation of a mouse model of necrotic granuloma
701 formation using C3HeB/FeJ mice for testing of drugs against Mycobacterium tuberculosis. *Antimicrob*
702 *Agents Chemother* 2012; **56**(6): 3181–95.
703 41. Rocca S, Schiavoni G, Sali M, et al. Interferon regulatory factor 8-deficiency determines massive
704 neutrophil recruitment but T cell defect in fast growing granulomas during tuberculosis. *PLoS One* 2013;
705 **8**(5): e62751.
706 42. Mehra S, Alvarez X, Didier PJ, et al. Granuloma correlates of protection against tuberculosis and
707 mechanisms of immune modulation by Mycobacterium tuberculosis. *J Infect Dis* 2013; **207**(7): 1115–27.
708 43. Herbert C, Luies L, Loots DT, Williams AA. The metabolic consequences of HIV/TB co-
709 infection. *BMC Infectious Diseases* 2023; **23**(1).

710 44. Masson JJR, Murphy AJ, Lee MKS, Ostrowski M, Crowe SM, Palmer CS. Assessment of
711 metabolic and mitochondrial dynamics in CD4+ and CD8+ T cells in virologically suppressed HIV-
712 positive individuals on combination antiretroviral therapy. *PLOS ONE* 30 ago 2017; **12**(8).
713 45. Singh V, Jamwal S, Jain R, Verma P, Gokhale R, Rao Kanury VS. Mycobacterium tuberculosis-
714 Driven Targeted Recalibration of Macrophage Lipid Homeostasis Promotes the Foamy Phenotype. *Cell*
715 *Host & Microbe* 2012/11/15; **12**(5).
716 46. Gern BH, Adams KN, Plumlee CR, et al. TGFβ restricts expansion, survival, and function of
717 T cells within the tuberculous granuloma. *Cell Host & Microbe* 2021; **29**(4): 594–606.e6.
718 47. Peters JM, Gideon HP, Hughes TK, et al. Systematic deconstruction of myeloid cell signaling in
719 tuberculosis granulomas reveals IFN-γ, TGF-β, and time are associated with conserved myeloid diversity.
720 *bioRxiv* 2024: 2024.05.24.595747.
721 48. Warsinske HC, Pienaar E, Linderman JJ, Mattila JT, Kirschner DE. Deletion of TGF-beta1
722 Increases Bacterial Clearance by Cytotoxic T Cells in a Tuberculosis Granuloma Model. *Front Immunol*
723 2017; **8**: 1843.

724